Fracturing controlled primary migration of hydrocarbon fluids during heating of organic-rich shales

Maya Kobchenko, Hamed Panahi, Francois Renard, Dag Kristian Dysthe, Anders Malthe-Sorenssen, Adriano Mazzini, Julien Scheibert, Bjorn Jamtveit, Paul Meakin

Fracturing controlled primary migration of hydrocarbon fluids during heating of organic-rich shales

Maya Kobchenko[1], Hamed Panahi[1,2], François Renard[1,3], Dag K. Dysthe[1], Anders Malthe-Sørenssen[1], Adriano Mazzini[1], Julien Scheibert[1], Bjørn Jamtveit[1] and Paul Meakin[1,4,5]

[1] Physics of Geological Processes, University of Oslo, Norway

[2] Statoil ASA, Oslo, Norway

[3] Institut des Sciences de la Terre, Université Joseph Fourier and CNRS, Grenoble, France

[4] Idaho National Laboratory, Idaho Falls, USA

[5] Institute for Energy Technology, Kjeller, Norway

Abstract

Time-resolved three-dimensional *in situ* high resolution synchrotron x-ray tomographic imaging was used to investigate the effects of slowly heating organic-rich Green River Shale from 60° to 400°C, in air without confinement, to better understand primary migration of hydrocarbon fluids in very low permeability source rock. Cracks nucleate in the interior of the sample at a temperature around 350°C. As the temperature increases, they grow and coalesce along lamination planes to form bigger cracks. This process is accompanied by a release of light hydrocarbons generated by decomposition of the initially immature organic matter, as determined by thermogravimetry and gas chromatography. These results provide the first 4D monitoring of an invasion percolation-like fracturing process in organic-rich shales. This process increases the permeability of the sample and provides pathways for fluid expulsion - an effect that might also be relevant for primary migration under natural conditions. We propose a 2D fracture model that reproduces both the observed non-linear crack growth in a lamination plane and the irregular geometry of the crack fronts.

1. Introduction

A wide variety of geological phenomena involve the generation and migration of fluids in low permeability rocks. For example, dehydration of sediments in subduction zones generates large fluxes of water that rise along low-permeability subduction interfaces, and provide a mechanism for creep and/or slow earthquakes [*Obara*, 2002]. Similarly, the illitization of clays at depth and the production of methane in organic-rich shales are responsible for the development of overpressure and the formation of piercement structures that are manifest on the surface as mud volcanoes [*Mazzini et al,* 2009]. The emplacement of magmatic bodies into sedimentary basins may also rapidly decompose organic matter, and the resulting gasses may migrate through low permeability rocks in quantities sufficient to bring about mass extinction due to global warming and ozone depletion [*Svensen et al.,* 2004].

Primary migration, *i.e.* the transport of hydrocarbon fluids from extremely low permeability source rocks in which they are generated to more permeable rocks through which they migrate to a trap (reservoir) or to the surface is an example of both economic and fundamental interest. As the organic-rich fine grained sediment from which the source rock is formed is buried, the organic material is transformed into complex high molecular weight/cross-linked organic oil and gas precursors (kerogen). On continued burial, the temperature and pressure rise, and kerogen decomposes into low molecular weight hydrocarbon fluids (gas and oil) which have a much lower viscosity than the kerogen. Part of the generated hydrocarbon fluids escape from the shale into secondary migration pathways, by processes that remain enigmatic, in spite of decades of investigation [*Bjorlykke, 2010*]. The rest is retained in the source rock explaining why shales are becoming an important source of unconventional hydrocarbon fuels, particularly natural gas [*Mohr*, 2010].

Fracturing is commonly cited as the most likely mechanism to increase the permeability of source rocks and provide pathways for the generated hydrocarbons [*Vernik*, 1994; *Berg and Gangi*, 1999; *Lash and Engelder*, 2005]. During kerogen decomposition, generation of less dense fluids leads to pore-pressure build-up, which may cause cracking of the host rock. The presence of microcracks in shales was highlighted by several authors [*Capuano*, 1993; *Marquez and Mountjoy*, 1996], based on 2D imaging techniques. Here we present the first *in situ* 3D experimental investigation of crack formation in organic-rich shale during kerogen decomposition. We show that the 3D crack fronts have complex irregular geometries, and that the fracture process is similar to invasion percolation.

Under natural conditions, this fracture process takes place at depths of several kilometers over millions of years, making its monitoring impossible. Therefore, it is very important to construct adequate models of primary migration. Recently, *Jin et al.* [2010] introduced a fracture mechanics model of subcritical crack propagation and coalescence, based on the assumption of linear elastic behavior of the rock. Although the model provides an estimate of the fracture propagation time, the geometry and mechanism of fracture formation were oversimplified. Here we propose a 2D fracture model, assuming short-ranged interactions only, which reproduces the complex crack front shape and the invasion-percolation-like fracturing process observed experimentally.

2. Characterization of Green River Shale samples

The samples were obtained from an outcrop of the organic-rich R-8 unit, of potential commercial interest, in the Green River Formation of the Piceance Basin in northwestern Colorado, USA. It was formed from Eocene lacustrine sediments [*Ruble et al.,* 2001], it presents well-developed lamination and anisotropic mechanical properties [*Vernik and Landis*, 1996] and it contains organic matter (total organic content 9.92 wt%) present in the form of patches of kerogen, distributed preferentially along lamination planes. Before the experiment, this shale had not been exposed to temperatures that would cause significant thermal maturation.

Cylindrical core samples (5mm height, 5mm in diameter) cut perpendicular to lamination were prepared for X-ray tomography. Thin sections were taken before and after heating. Thin section microscopy (optical, scanning electron microscopy [SEM]) was performed to map micro-structural features. Optical microscope images highlight the micro-fabric of the shale consisting of alternating light colored carbonate and pyrites-rich lamina with darker clay-rich intervals. Organic-matter can be observed as dark lenses, which are laterally extensive or localized within the clayey and micrite-rich layers (Figure 1A-B). SEM on carbon-coated thin sections using back-scattered electron imagery [BSE] with X-ray spectroscopy was used to identify the elemental composition of the minerals in the matrix. The rock matrix consists of detrital mineral grains with diameters ranging between 10-50 μm, with clay-rich micritic calcite filling the pores in the groundmass. The largest mineral grains are recognized as quartz, pyrites, carbonates and feldspar crystals (Figure 1D).

Thermogravimetry [TGA] coupled with gas chromatography-mass spectrometry [GC-MS] was used to analyze the outgoing products during heating, and to determine the temperature of catagenesis. Using TGA, we monitored mass loss of the sample during heating at 10°C/min in air or nitrogen. GC-MS gave information about the amount of outgoing hydrocarbons, water and carbon dioxide during heating at 5°C/min in air or nitrogen. Water release was almost constant between 200 and 1000°C. Carbon dioxide and hydrocarbon emission and mass loss in the thermogravimetry diagram started at around 350°C.

3. Time-lapse 3D imaging and data processing

X-ray tomographic 3D imaging of the shale samples was carried out using beamline ID19 at the European Synchrotron Radiation Facility (ESRF) in Grenoble, France. This non-invasive imaging technique measures the absorption of X-rays, to produce a 3D map of X-ray attenuation. The experimental equipment includes a sample manipulator for alignment, a rotation stage for the tomography scan and a high resolution imaging X-ray detector. The 3D data were obtained at a voxel resolution of $5\mu m^3$ at a beam energy of 20 keV.

The prepared cylinder was located in a home-built furnace in contact with air, with no confining pressure, and it was gradually heated *in-situ* from 60°C to 400°C at approximately 1°C/min. 28 time-lapse scans of this sample were acquired during the heating phase, then several at 400°C. Each scan required 11-14 minutes, and a new scan was started immediately afterwards. Several other samples were imaged before and after heating only, and used to test experimental reproducibility. For all scans, 1500 radiographs were acquired while the sample was rotated over 180°. Based on the sets of radiographs, a filtered back-projection reconstructing algorithm was used to calculate the 3D raw-tomograms representing the microporous structure of the sample at different stages of heating. The final 3D volumes were represented by raw files of 830^3 voxels coded in 8-bit gray levels.

The 3D images were processed in two ways. First, the strain field both along and perpendicular to lamination were measured, in a typical 2D centered vertical slice of the volume, using digital image correlation [*Hild and Roux*, 2006]. Second, in order to determine crack geometries and track crack propagation, the shape, volume and morphology of the cracks was analyzed in 3D using an imaging software package (AvizoFire ©). Quantitative analysis of the crack formation required isolation of the cracks from the rock matrix. Due to the small crack opening (3-4 voxels), the following procedure was applied: first a binary mask was used to delete the background and the central noisy part of the volumes (imaging artifact); then, an edge-preserving smoothing filter based on Gaussian smoothing combined with a non-linear diffusion algorithm was applied; and finally a "watershed" procedure enabled individual cracks to be isolated [*Sonka et al*, 1999]. The final result of the segmentation process is a series of cracks represented by connected voxels, marked by different labels (represented in different colors in Figure 2A).

4. Observation of deformation and crack formation

A set of thin sections and the tomography images were studied in order to compare petrographic and morphological characteristics of the shale before and after heating. Before heating, organic precursors, which are preferentially oriented parallel to the lamination can be distinguished throughout the sample in the thin section optical images (Figure 1A-B). The color of the shale matrix in the optical images of thin sections after heating was lighter than that before heating due to the loss of organics. Also an abundance of cracks, partially filled with residual organic material, was distributed parallel to the lamination.

Tomographic scans of unheated samples identified the densest grains (pyrites) of the shale matrix, which appear as bright inclusions (Figure 1C). The presence of these grains enabled deformation of the sample to be monitored and strain variations to be measured during heating. The analysis of the time lapse 3D imaging during heating revealed two distinct deformation regimes: first the sample expanded almost homogenously, and then the deformation abruptly localized at open cracks. The 2D correlation analysis showed different strain evolutions with temperature depending on the direction. Strain along lamination increased linearly with temperature from 0 at 60°C to 0.6% at around 350°C (just before cracks appeared). Strain perpendicular to lamination increased almost linearly from 0 at 60°C to 1.2% at 290°C, before increasing rapidly to 1.9% at around 350°C.

3D image analysis was then performed to determine the geometry of propagating cracks. Figure 2A shows a 3D rendering of the fracture pattern at T=391°C and Figures 2B and 2C show a cut perpendicular to the lamination. The general direction of crack propagation follows lamination planes (no perpendicular fracture was observed). They have essentially constant aperture widths (typically 15-20 micrometers) and rough surfaces in both the horizontal and vertical planes. Figure 3 shows the time evolution of crack propagation in a given lamination plane. As the temperature rises, cracks nucleate, grow and coalesce in a quasi-static manner until they almost fill the plane. Pyrite grains, which can be seen as bright spots in the tomography images (Figure 2C), affect crack growth by pinning the crack front, and control the out-of-plane excursions of the crack path.

5. Discrete model of crack propagation

Based on the fracturing behavior observed during the experiments, a 2D model of in-plane crack nucleation and growth during shale maturation was developed. The model contains the minimum number of components needed to reproduce the key characteristics of the crack growth process (see Supplementary Material). The model focuses on a layer of shale that fractures more rapidly than nearby layers because it has higher kerogen content and/or it is weaker. The layer is modeled by a regular square lattice in which every site represents a small organic-rich shale element. The temperature rises gradually with time and kerogen decomposes, causing a progressive pressure build-up. Each site is characterized by a breaking threshold $\sigma_{c,i}$, and when the pressure exceeds this threshold $p_i > \sigma_{c,i}$, the site breaks and either nucleates a new crack or increases the size of a pre-existing crack. This relaxes the stress, which is distributed equally to the nearest neighbours (long-range elastic interactions are neglected), bringing them closer to failure. This was implemented by reducing the breaking threshold, $\sigma_{c,i} \rightarrow \sigma_{c,i} - d\sigma$, for all nearest neighbors. Each crack is represented by a cluster of broken sites. As soon as sites belonging to different clusters become adjacent, both clusters are merged to form a single crack, and all the merged sites are given the same label/color.

Figure 4A shows three successive snapshots during a simulation. In the early stage, the system contains many small independent cracks. Each crack has a rough front, and over time, individual cracks grow slowly and merge until the whole plane is covered. Figure 4B displays the increase of the surface area of the largest final simulated crack. Crack growth occurs in three stages: (1) the fractures are all separated and their surface areas grow gradually; (2) the fractures start to connect and their areas increases in small jumps; and (3) after some time, the system is dominated by one large fracture, with an area that grows by intermittent increases. This intermittent growth dynamics is similar to the behavior of cellular automata earthquake models [*Bak*, 1987] and the crack pattern grows like those produced by invasion percolation processes [*Dias and Wilkinson*, 1986].

We suggest that this local deformation approach to the modeling of crack propagation in tight rocks can be applied to other geological systems in which chemical reactions induce volume increase and stress build-up within the rocks. These systems are widespread, including weathering of rocks near the surface [*Røyne et al*., 2008], dehydration of serpentines in subduction zones [*Jung et al.,* 2004] and primary migration of hydrocarbons.

6. Discussion and conclusion

Fracturing during fluid generation in a tight organic-rich rock (oil shale) was investigated experimentally using thin section imaging (optical and SEM), gas chromatography, thermogravimetry and 3D x-rays tomography. At temperatures below ≈300ºC degrees, the sample undergoes a simple linear expansion, with an anisotropy related to the rock lamination. Above 300ºC, the expansion perpendicular to lamination significantly accelerates up to a temperature of ≈350ºC, the temperature at which the first cracks can be detected on the 3D images. Thermogravimetry analysis indicates rapid mass loss in the same temperature range, and chromatography of the outgoing gas indicates kerogen decomposition.

Time-resolved high-resolution synchrotron x-rays tomography allowed us to follow the dynamics of the fracturing process accompanying hydrocarbon expulsion. At 350ºC, many small cracks were nucleated. With continued heating and kerogen decomposition, cracks grow parallel to lamination and coalesce, until a percolating crack network spanning a single lamination plane has formed. This process occurs simultaneously on different lamination planes. In our experiments, cracks propagate due to heating. However, we emphasize that the crack propagation mechanism we observed might be of much wider relevance since nucleation, growth and coalescence has been observed in a large variety of heterogeneous rocks under different loading conditions (see e.g. [*Moore and Lockner*, 1995]).

The analysis of the evolution of the area of the biggest crack in a given lamination plane (Figure 4C) shows a very slow initial increase followed by a rapid increase as cracks coalesce. We managed to qualitatively reproduce this behavior (Figure 4B) with a 2D model, based on the assumption of nearest-neighbor stress transfer upon cracking. The crack patterns are similar to the irregular crack fronts observed in the experiment and the non-linear crack growth also occurs through the sudden merging of individual cracks.

Our results provide the first 4D monitoring of an invasion percolation-like fracturing process in organic-rich shale. Most likely, cracks are caused by local volume increase and stress generation produced by organic matter decomposition. These growing and coalescing cracks enhance the permeability of the sample and the hydrocarbon fluids generated by kerogen decomposition can escape through the dynamically created pathways. Similar mechanisms might be relevant for primary migration under natural conditions.

Several questions remain open. What is the origin of the anomalous vertical thermal expansion of the sample between 300 and 350°C, well before any crack can be detected on the images? It might be the signature of the nucleation of microcracks with a size much smaller that the spatial resolution of our 3D imaging, throughout the volume of the sample. What would be the effect of stress and/or confinement similar to that in natural environments? It would probably cause the fractures to close once the fluid has escaped, making it difficult to identify the fracture network in exhumed rock samples.

Acknowledgments. The present study was supported by the Petromaks program of the Norwegian Research Council. We would like to thank Elodie Boller at ESRF for her help during the tomography scans.

References

Bak, P. (1996), How Nature Works: The Science of Self-Organized Criticality, *New York, USA.*

Bjørlykke, K. (2010), Petroleum Geoscience: From Sedimentary Environments to Rock Physics, *Springer, Berlin, Germany.*

Berg, R.R., and A.F. Gangi (1999), Primary migration by oil-generation microfracturing in low-permeability source rocks: application to the Austin Chalk, Texas, *AAPG Bull., 83, 727-756.*

Capuano, R.M. (1993), Evidence of fluid flow in microcracks in geopressured shales, *AAPG Bull., 77, 1303-1314.*

Dias, M. M., and D. Wilkinson (1986), Percolation with trapping, *J. Phys. A. Math. Gen.,*19, 3131.

Hild, F., and S. Roux (2006), Digital Image Correlation: from Displacement Measurement to Identification of Elastic Properties – a Review, *Strain, 42, 69-80.*

Jin, Z.-H., S. E. Johnson, and Z. Q. Fan (2010), Subcritical propagation and coalescence of oil-filled cracks: Getting the oil out of low-permeability source rocks, *Geophys. Res. Lett., 37,* L01305

Jung, H. (2004), Intermediate-depth earthquake faulting by dehydration embrittlement with negative volume change, *Nature, 428, 6982, 545-549.*

Lash, G.G., and T. Engelder (1992), An analysis of horizontal microcracking during catagenesis: Example from Catskill delta complex, *AAPG Bull., 89, 1433-1449.*

Marquez, X.M., and E.W. Mountjoy (1996), Microcracks due to overpressure caused by thermal cracking in well-sealed Upper Devonian reservoirs, deep Alberta basin, *AAPG Bull., 80, 570-588.*

Mazzini, A., Svensen, H., Planke, S., Guliyev, I., Akhmanov, G.G., Fallik, T., and Banks, D., (2009), When mud volcanoes sleep: Insight from seep geochemistry at the Dashgil mud volcano, Azerbaijan, *Marine and Petroleum Geology, 26, 1704-1715.*

Mohr, S., and G. Evans (2010), Long term prediction of unconventional oil production, *Energy policy, 38, 265-276.*

Moore, D. E. and Lockner, D.A. (1995) The role of microcracking in shear-fracture propagation in granite, *J. Struct. Geol., 17, 95-114*

Obara, K. (2002), Nonvolcanic deep tremor associated with subduction in southwest Japan, *Science, 296, 1679-1681.*

Røyne, A., Jamtveit, B., Mathiesen, J., and Malthe-Sorrenssen A. (2008), Controls of rock weathering rates by reaction-induced hierarchical fracturing, *Earth Planet. Sci. Lett., 275, 364-369*.

Ruble, T. E., M.D. Lewan, and R.P. Philp (2001), New insights on the Green River petroleum system in the Uinta basin from hydrous pyrolysis experiments, *AAPG Bull., 85, 1333 -1371.*

Sonka, M., Hlavac, V., and R. Boyle (1999), Image processing, analysis and machine vision, *PWS Publishing, Pacific Grove, CA, USA.*

Svensen, H., Planke, S., Malthe-Sorenssen, A., Jamtveit, B., Myklebust, R., Eidem, T.R., and S.S.Rey (2004), Release of methane from a volcanic basin as a mechanism for initial Eocene global warming, *Nature, 429, 6991, 542-545.*

Vernik, L. (1994), Hydrocarbon-generation-induced microcracking of source rocks, *Geoph., 59, 555-563.*

Vernik, L., and C. Landis (1996), Elastic anisotropy of source rocks: Implications for hydrocarbon generation and primary migration, *AAPG Bull., 80, 531-544.*

Figure 1: Finely laminated Green River Shale samples before heating. (A) Optical image of interlaminated silt and clay minerals. (B) Enlarged optical image of a kerogen patch located between silt grains. (C) X-ray tomography slice of the sample, perpendicular to lamination. Bright spots are pyrites grains. (D) Back scattered electron micrograph of silt layer including cracks filled with organics (arrows) surrounded by feldspar (f), pyrite (p), carbonate (c) and quartz (q) grains.

Figure 2: Tomography images of the shale sample after heating. (A) 3D rendering of final crack network. Each crack corresponds to a different color. (B) 2D slice showing (dark) elongated cracks parallel to the bedding. The central vertical noisy line is an artifact of the micro-tomography technique. (C) Enlargement of (B) showing a crack around a grain of pyrite (arrow).

Figure 3:

Crack propagation dynamics in a lamination plane. (A) Many small cracks nucleated around 350°C. Each crack has a different color. (B) Cracks grow with temperature. (C) At some critical stage all cracks have merged into a single sample-wide crack. The circular central region was removed because of a data acquisition artifact.

Figure 4:

2D model of primary migration-related fracturing. (A) Three stages of the evolution: nucleation, growth and percolation of cracks. (B) Growth of the area of the biggest crack as a function of time (i.e. kerogen reaction progress). (C) Analogous evolution in a lamination plane in the experiment. The decrease observed after temperature 390°C corresponds to partial crack closing after fluid expulsion.

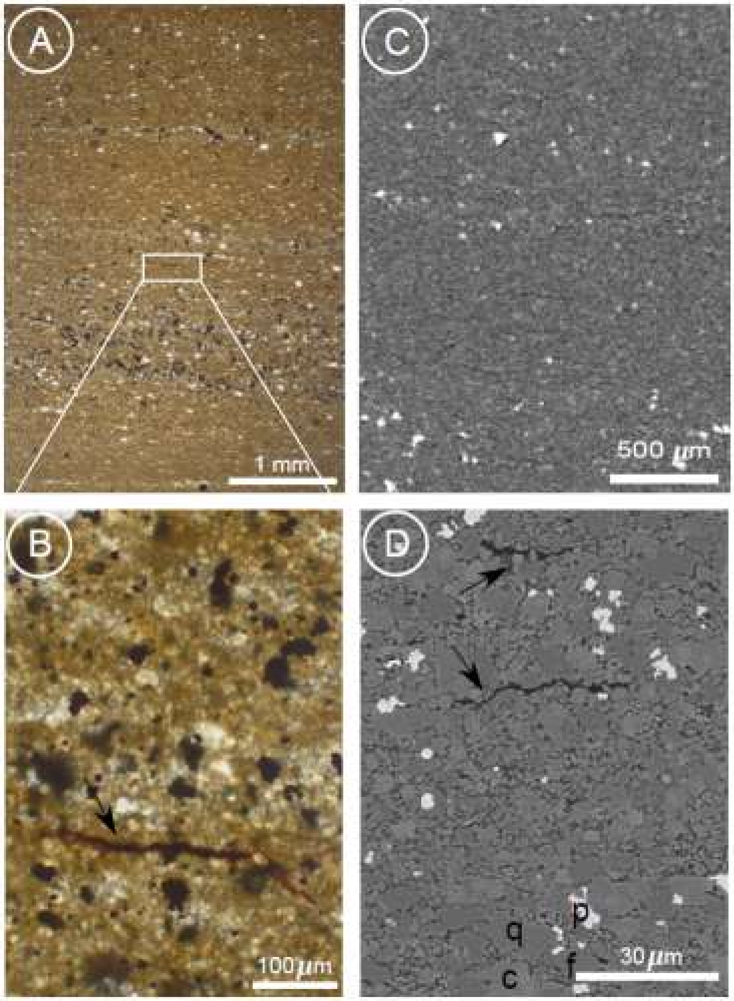

Figure 1

295 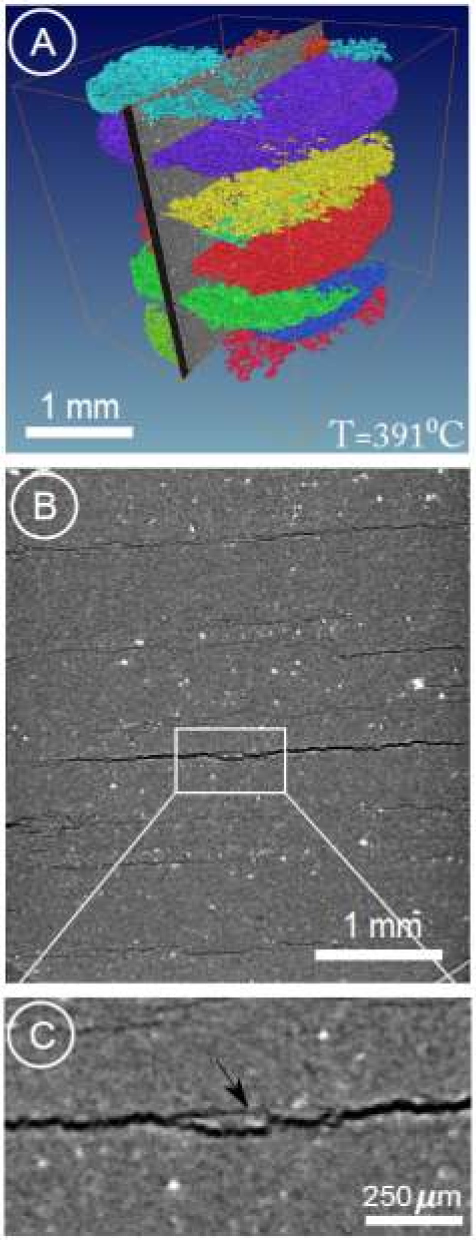

296 **Figure 2**

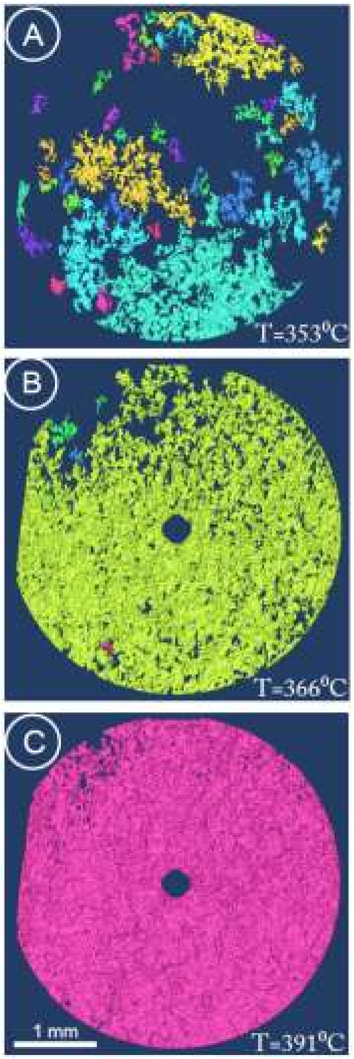

Figure 3

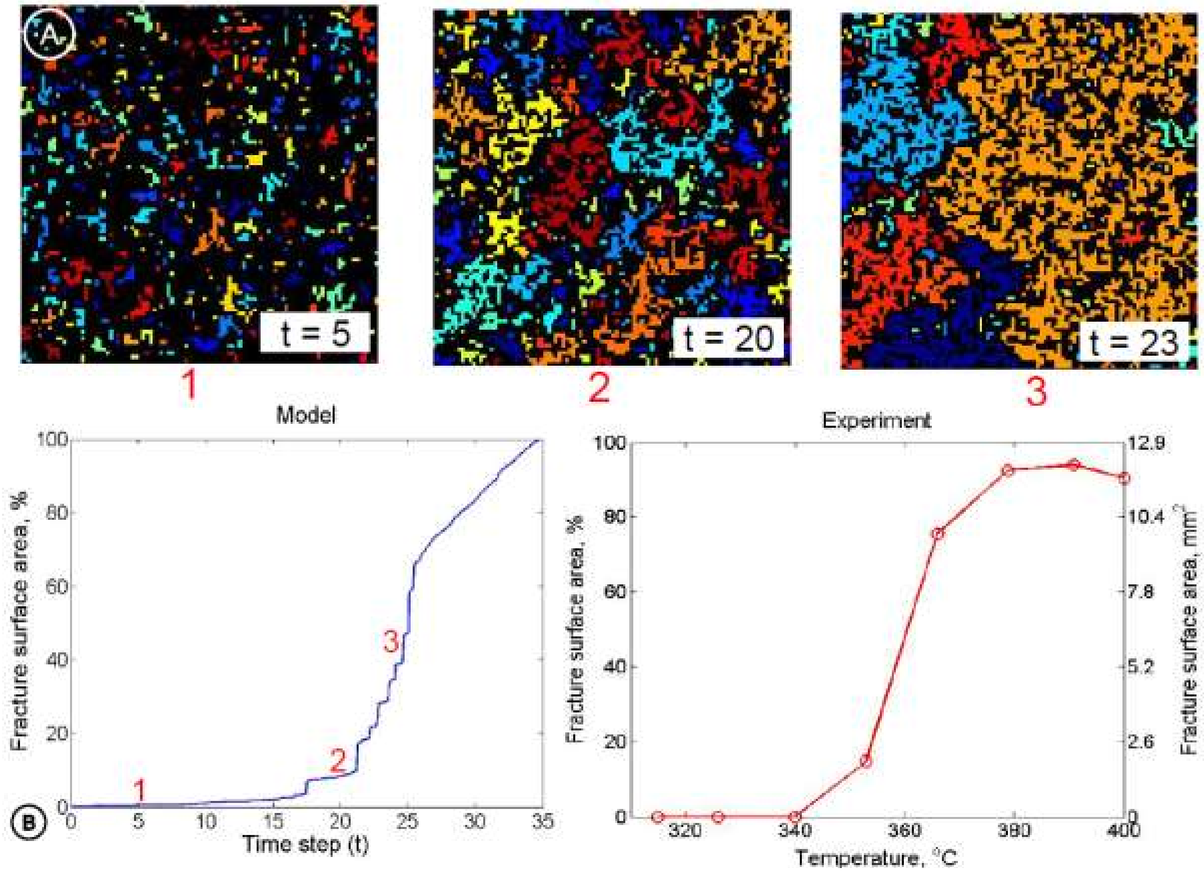
A
t = 5
t = 20
t = 23
1
2
3
Model
Experiment
B
Fracture surface area, %
Time step (t)
Temperature, °C
Fracture surface area, mm²

Figure 4